Ocean Dynamics are Key to Extratropical Forcing of El Niño

SOUMI CHAKRAVORTY,[a,b] RENELLYS C. PEREZ,[b] BRUCE T. ANDERSON,[c] SARAH M. LARSON,[d] BENJAMIN S. GIESE,[e] AND VALENTINA PIVOTTI[c]

[a] *Cooperative Institute for Marine and Atmospheric Studies, University of Miami, Miami, Florida*
[b] *NOAA/Atlantic Oceanographic and Meteorological Laboratory, Miami, Florida*
[c] *Department of Earth and Environment, Boston University, Boston, Massachusetts*
[d] *Department of Marine, Earth, and Atmospheric Sciences, North Carolina State University, Raleigh, North Carolina*
[e] *Center for Coastal Studies, Provincetown, Massachusetts*

(Manuscript received 4 December 2020, in final form 26 July 2021)

ABSTRACT: El Niño–Southern Oscillation (ENSO) has been recently linked with extratropical Pacific Ocean atmospheric variability. The two key mechanisms connecting the atmospheric variability of the extratropical Pacific with ENSO are the heat flux–driven ''seasonal footprinting mechanism'' (SFM) and the ocean dynamics–driven ''trade wind charging'' (TWC) mechanism. However, their relative contributions to ENSO are still unknown. Here we present modeling evidence that the positive phase of the SFM generates a weaker, short-lived central Pacific El Niño–like warming pattern in the autumn, whereas the TWC positive phase leads to a wintertime eastern Pacific El Niño–like warming. When both mechanisms are active, a strong, persistent El Niño develops. While both mechanisms can trigger equatorial wind anomalies that generate an El Niño, the strength and persistence of the warming depends on the subsurface heat content buildup by the TWC mechanism. These results suggest that while dynamical coupling associated with extratropical forcing is crucial to maintain an El Niño, thermodynamical coupling is an extratropical source of El Niño diversity.

KEYWORDS: Atmosphere–ocean interaction; El Niño; Extratropics; Climate models

1. Introduction

El Niño–Southern Oscillation (ENSO) is a dominant source of climate variability (Chakravorty et al. 2013, 2016; Lau and Nath 1996) generated by coupled ocean–atmosphere processes in the tropical Pacific Ocean (Cane and Zebiak 1985; Jin 1997). ENSO is a cycle of central and eastern equatorial Pacific warming (referred to as El Niño) and cooling (referred to as La Niña). Although generally confined to the tropics, some of the strongest ENSO events in recent history have been influenced by low-frequency extratropical Pacific atmospheric variability (Amaya et al. 2019; Lu et al. 2017). Further, some aspects of ENSO diversity arise from extratropical atmospheric variability (Pegion et al. 2020). Thus, understanding the influence of extratropical climate variability on the tropical Pacific is a crucial aspect of ENSO predictability (Larson et al. 2018a) and forecast skill (Tippett et al. 2012). A key source of extratropical atmospheric variability is the North Pacific Oscillation (NPO) (Rogers 1981), which influences subsequent boreal winter ENSO development and serves as a potential predictor of ENSO one year in advance (Amaya et al. 2019). In particular, the positive phase of the NPO (+NPO) initiates the El Niño, via the thermodynamically coupled ''seasonal footprinting mechanism'' (SFM; Vimont et al. 2003, 2009). As part of the +SFM, the southern lobe of +NPO weakens the North Pacific trade winds during winter. Through the wind–evaporation–sea surface temperature (WES) feedback, the weakened easterly trade winds generate sea surface temperature (SST) warming that extends from the eastern subtropical Pacific southwestward to the western equatorial Pacific, called the North Pacific meridional mode (NPMM) Chiang and Vimont 2004). This SST ''footprint'' (Vimont et al. 2003, 2009) persists until the following summer and subsequently interacts with the overlying atmosphere, inducing southwesterly wind anomalies on the southern edge of the surface warming. This relaxes the climatological trades over the western equatorial Pacific and can excite an oceanic response that triggers an El Niño the following winter (Amaya et al. 2019; Pegion and Alexander 2013; Vimont et al. 2003).

In contrast, +NPO can also dynamically link extratropical atmospheric variability with El Niño through the ''trade wind charging'' (TWC) mechanism (Anderson 2007; Anderson et al. 2013; Anderson and Perez 2015; Chakravorty et al. 2020). Westerly wind anomalies associated with the southern lobe of the +NPO produce an off-equatorial wind stress curl that drives equatorward upper ocean mass transport (Anderson and Perez 2015; Clarke et al. 2007). The central equatorial Pacific Ocean is then charged with warm water (Anderson 2007; Anderson et al. 2013; Anderson and Perez 2015), priming the system for an El Niño (Jin 1997; Wyrtki 1985). These warm waters then advect eastward and upward along the equatorial thermocline and outcrop in the eastern Pacific, creating El Niño favorable conditions upon which coupled air–sea feedbacks can act (Anderson 2007; Anderson et al. 2013; Anderson and Perez 2015). In a coupled model study, Chakravorty et al. (2020) demonstrated that coupled air–sea feedbacks indeed amplify +TWC-induced surface and subsurface warming, oftentimes resulting in an El Niño the following winter.

That said, El Niño exhibits considerable spatiotemporal variability, a manifestation of ENSO diversity. One of the most important markers of ENSO diversity is the longitudinal location of the peak SST anomaly—that is, canonical or cold tongue El Niño events with eastern Pacific warming versus

Corresponding author: Soumi Chakravorty, soumi.chakravortyhb@gmail.com

DOI: 10.1175/JCLI-D-20-0933.1

© 2021 American Meteorological Society. For information regarding reuse of this content and general copyright information, consult the AMS Copyright Policy (www.ametsoc.org/PUBSReuseLicenses).

Brought to you by NOAA Central Library | Unauthenticated | Downloaded 10/12/21 03:47 PM UTC

central or west Pacific El Niño events (Ashok et al. 2007; Yu and Kim 2011) where SST warming is mainly concentrated over the central equatorial Pacific. Eastern and central Pacific El Niño events feature distinctly different associated surface and subsurface anomaly evolution in the tropical Pacific (Kao and Yu 2009; Yu and Kim 2010; Chakravorty et al. 2021, manuscript submitted to *J. Geophys. Res.*), which leads to radically different climatic impacts (Capotondi et al. 2015; Infanti and Kirtman 2016; Lee et al. 2018; P. Wang et al. 2019) and limits ENSO predictability (Ineson et al. 2018; McPhaden 2015). Some aspects of ENSO diversity arise from extratropical atmospheric variability (Pegion et al. 2020). Studies have found that the formation of eastern Pacific (EP) El Niño events is best explained by tropical Pacific air–sea coupled processes (Battisti and Hirst 1989; Wyrtki 1985; Jin 1997), whereas the initiation of central Pacific (CP) El Niño events has been linked to extratropical variability (Yu and Kim 2011; Yu et al. 2017; Pegion et al. 2020). However, Chakravorty et al. (2020) found that extratropical atmospheric forcing through the +TWC mechanism generated EP-like El Niño events. Hence, it is unclear whether +NPO favors a particular El Niño type, and there remains considerable uncertainty with regard to processes that are crucial for El Niño development. Although the SFM and TWC mechanisms are potential predictors of ENSO, their individual and combined contributions to its evolution and diversity still need to be examined. Thus, identifying and understanding how extratropical atmospheric variability influences the tropical Pacific through these two different mechanisms is crucial to improving ENSO predictability (Larson et al. 2018a; Pegion et al. 2020).

Here, we test the relative roles of the positive SFM and TWC mechanisms on El Niño generation using a coupled model experimental framework. Section 2 provides details of the model framework and experimental design. The results, obtained from different sensitivity experiments, are presented in section 3. A summary of the key results and a discussion of the implications for ENSO diversity are provided in section 4.

2. Methods

Model framework and experiments

The coupled model framework used here follows Chakravorty et al. (2020), who explored the influence of the TWC on ENSO, with some suitable modifications described below. The coupled model is the coupled National Center for Atmospheric Research (NCAR) Community Earth System Model, version 1.2.2.1 (CESM1; Hurrell et al. 2013; X. Wang et al. 2019), configured with the Parallel Ocean Program, version 2 (POP2; Smith et al. 2010), ocean model with 60 vertical levels and 1° × 1° resolution globally and 0.3° meridional resolution near the equator. The atmospheric model is the Community Atmosphere Model, version 5 (CAM5; Gettelman et al. 2010), with 0.9° × 1.25° resolution and 30 vertical layers. CESM1 is integrated in fully coupled mode for 222 years from a 500-yr spinup run with preindustrial (1850) radiative forcing, hereinafter referred to as the control simulation. The control simulation is used to identify 30 suitable 1 November initial conditions and to calculate the climatological boundary conditions for the sensitivity experiments (the selection criteria for the ENSO-neutral initial conditions are discussed in the appendix).

To isolate the effect of +TWC and +SFM on generating ENSO events, we used an idealized two-step model framework following Chakravorty et al. (2020). We initially forced the ocean component of the model with either +SFM or +TWC forcing from 1 November in year 0 to 30 April in year 1 (as the NPO dominates during boreal winter), hereinafter referred to as the forced stage. Then, from 1 May in year 1 to 31 March in year 2, we integrated the model unconstrained under full coupling [similar to the methods employed in Larson et al. (2018a); Larson and Kirtman 2015, 2017, 2019] in what we term the coupled stage (Figs. 1a,b). Note that in Chakravorty et al. (2020) an intermediary climatology forced stage preceded the coupled stage, but that intermediary stage began to prematurely damp the +SFM and +TWC generated anomalies and was deemed unnecessary for these experiments.

We perform ensemble experiments starting with 30 ENSO-neutral November initial conditions in which the forced stage consists of either the +TWC-related wind stress anomalies (+TWC ensemble experiment; Fig. 1c) or +SFM-related net heat flux anomalies (+SFM ensemble experiment; Fig. 1d) anomalies, generated using the observationally constrained 20CRv2c and SODAsi.3 reanalysis products (Carton and Giese 2008; Chakravorty et al. 2020; Giese et al. 2016) and superimposed on the climatological fluxes (calculated from the control simulation). The selection of ENSO-neutral initial conditions and the method used to generate the imposed forcing are briefly discussed in the appendix. For additional details see Chakravorty et al. (2020).

To examine the combined influence of the +SFM and +TWC, we conduct a third experiment, +(SFM + TWC) ensemble, in which both of the anomalous forcings are superimposed onto the climatological forcing fields during the forced stage. As in the real world, the NPO forces the tropical Pacific through both dynamic and thermodynamic processes; hence, this experiment will provide a more realistic representation of the +NPO influence on ENSO. As a baseline neutral state with which to compare our experiments, we perform a fourth experiment in which the ocean is forced with only climatological fluxes during the forced stage (the CLIM ensemble experiment). In the CLIM experiment, all coupled variability is suppressed in the forced stage such that any ENSO events that develop can only be attributed to internal variability occurring during the coupled stage (Larson et al. 2018a; Larson and Kirtman 2015). For all experiments, anomalies are computed with respect to the CLIM experiment in which only climatological forcing was applied in the forced stage.

3. Results

a. Controlled flux stage

In Fig. 2, we compare the ensemble-mean surface and subsurface anomalies during spring generated directly by the imposed forcing. The +SFM (Fig. 2a) generates warm SST anomalies (SSTA) over the subtropical North Pacific with a meridionally tilted structure characteristic of the NPMM. The associated positive sea surface height anomalies (SSHA), a

Brought to you by NOAA Central Library | Unauthenticated | Downloaded 10/12/21 03:47 PM UTC

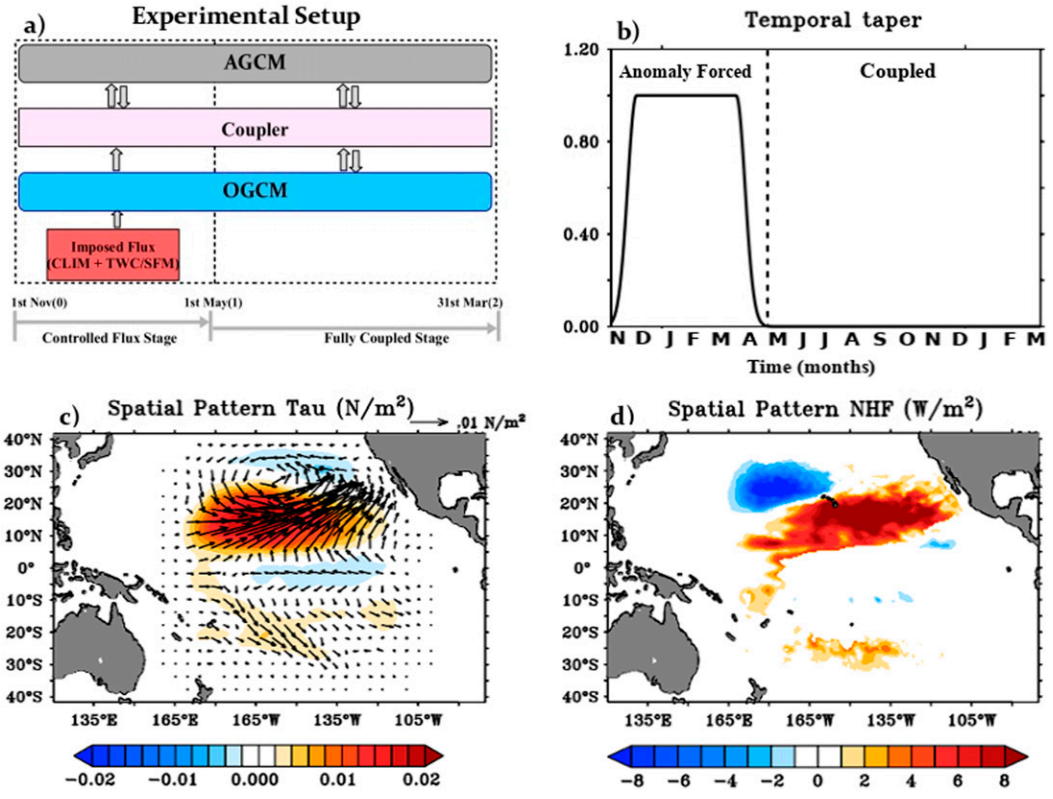

FIG. 1. (a) Schematic of the model experimental setup. (b) Time evolution of the forcing applied during the controlled flux stage (from November of year 0 to April of year 1) and the fully coupled stage of the experiments (from May of year 1 to March of year 2). (c) The spatial pattern of wind stress forcing related to the positive trade wind-charging (+TWC) added to the climatological forcing and applied to each ensemble member during the controlled flux stage. Total wind stress anomalies (N m^{-2}; vectors) are scaled to the reference vector in the top-right corner; zonal wind stress anomalies (N m^{-2}; shaded) correspond to the color bar on the bottom of the plot. (d) As in (c), but for the net heat flux forcing (W m^{-2}) related to the positive seasonal footprinting mechanism (+SFM).

proxy for subsurface warming, results from the accompanying thermal expansion (Fig. 2b). The wind stress anomaly is zero by design during the forced stage of this experiment. As expected, there is little subsurface warming over the equatorial Pacific (Fig. 2c) due to the lack of an ocean dynamic response.

The +TWC, unlike the +SFM, charges the equatorial Pacific with warm water (Chakravorty et al. 2020) and quickly generates strong subsurface warming (Fig. 2f). The imposed off-equatorial westerly anomalies, combined with anomalous equatorial easterlies, generate off-equatorial anticyclonic wind stress curl over the central Pacific (Fig. 2e) that induces downward Ekman pumping and deepens the off-equatorial thermocline, reflected by the positive SSHA (Fig. 2e). This results in equatorward mass transport (Anderson and Perez 2015; Chakravorty et al. 2020; Clarke et al. 2007) that increases subsurface temperatures along the central equatorial Pacific (Fig. 2f). The accumulation of warm water represents a ''charged'' equatorial Pacific state.

In the presence of combined forcing in the +(SFM + TWC) experiment (Fig. 2g), the ocean response is approximately a linear combination of the response to the individual forcing. Over the extratropical Pacific, +TWC generates warming superimposed on the +SFM forced NPMM SST anomaly pattern and strengthens the warming (Fig. 2g). Along the equatorial Pacific, the subsurface temperature and SSH anomalies (Figs. 2h,i) are almost identical to the structure and strength of the anomalous response in the +TWC experiment (Figs. 2e,f), consistent with the fact that the +SFM alone is unable to create a substantial subsurface thermal anomaly in the tropical Pacific (Figs. 2b,c).

b. *Fully coupled stage*

Next, we allowed the anomalies generated during the forced stage of the experiments to evolve freely in the presence of air–sea coupling (coupled stage) to explore the effectiveness of extratropical forced anomalies in generating an El Niño the following winter [November and December of year 1 and January of year 2: NDJ(1/2)].

In the +SFM experiment, the warm off-equatorial SST anomalies over the North Pacific begin to interact with the overlying atmosphere and generate southwesterly wind anomalies south of the warming in early summer (May–June of year 1; Fig. 3a). This weakens the prevailing northeasterly trades, resulting in reduced latent heat loss from the ocean and, through positive WES feedback, causes a local SST

Brought to you by NOAA Central Library | Unauthenticated | Downloaded 10/12/21 03:47 PM UTC

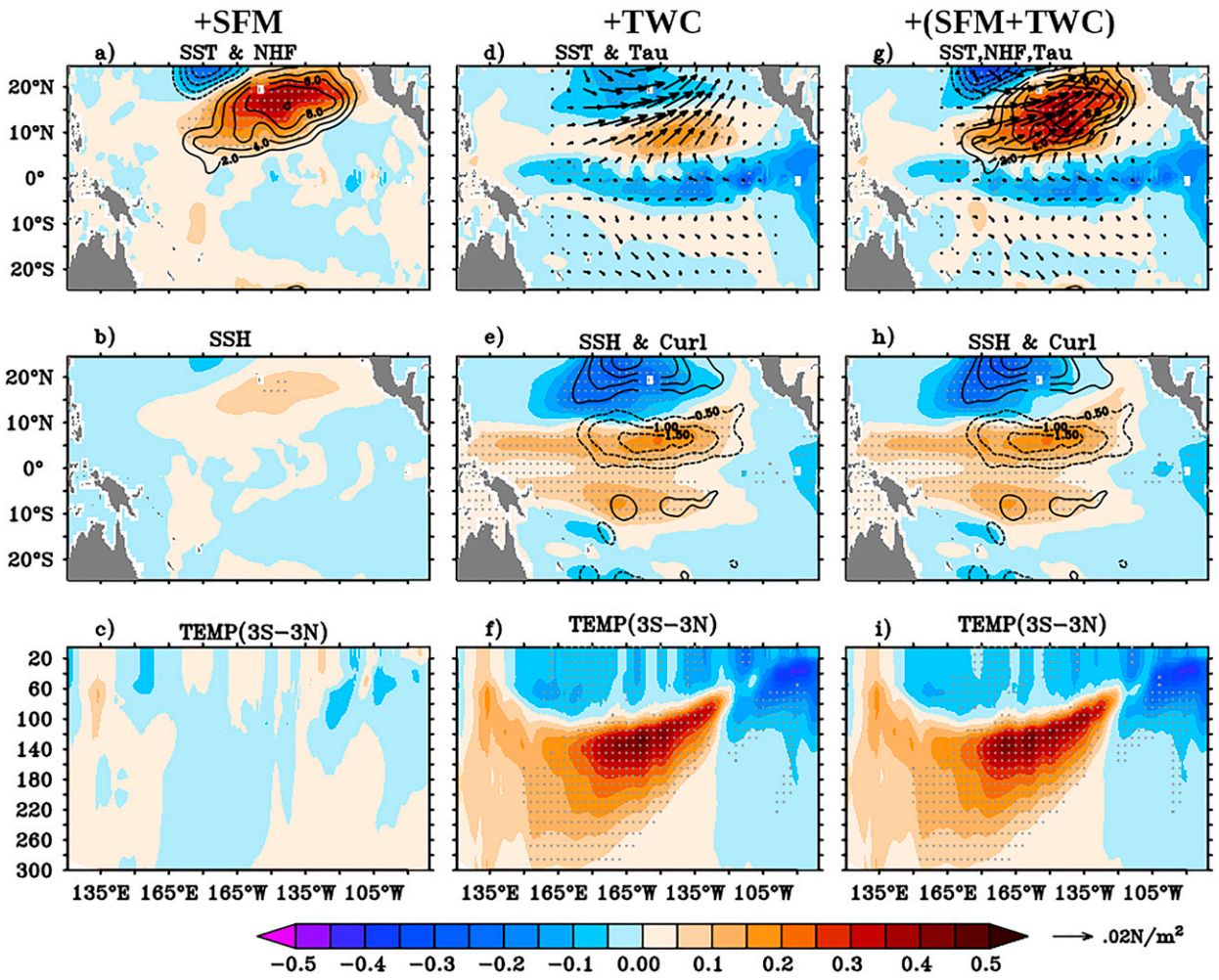

FIG. 2. Ensemble mean model response to (left) +SFM net heat flux forcing, (center) +TWC wind stress forcing, and (right) both forcings together during the forced stage relative to the CLIM ensemble means in March during year 1: (a) sea surface temperature (SST; °C; shading) and net heat flux (NHF; W m^{-2}, contours); (b) sea surface height (SSH; m; shading); (c) meridionally averaged (3°N–3°S) temperature anomalies for +SFM; (d) SST (°C; shading), wind stress, and tau (N m^{-2}; vectors) scaled to the reference vector in the bottom-right corner; (g) as in (d), but also including NHF (W m^{-2}; contours); (e),(h) SSH (m; shaded) and wind stress curl (10^{-8} N m^{-3}; contours with values ±0.3, ±0.5, ±1, ±1.5, and ±2); and (f),(i) meridionally averaged (3°N–3°S) temperature anomalies. Stippling indicates regions where the ensemble mean differences are significant with 90% confidence from a two-tailed Student's *t* test.

warming (Fig. 3a). This thermodynamically coupled feedback, along with a forced Rossby wave response, subsequently shifts the SST warming southwestward, warming the tropical northwestern Pacific by late summer (July–August of year 1; Fig. 3b). At the same time, significant positive SST and westerly wind anomalies form in the western and central equatorial Pacific (Fig. 3b). The off-equatorial northwest Pacific SST warming in late summer, combined with the seasonal northward shift of the intertropical convergence zone (ITCZ), drive the main precipitation band northward, resulting in a large off-equatorial atmospheric heat source (Gill 1980) in the western Pacific. This ''summer deep convection'' response (Amaya et al. 2019) generates anomalous westerlies in the western Pacific (Fig. 3b). These westerly wind anomalies weaken the prevailing equatorial easterlies and induce a weak (~0.3°C) warming over the central equatorial Pacific with a structure characteristic of a CP El Niño (Fig. 3c) that peaks in the fall (September–October of year 1).

From fall to winter of year 1, weakening of the northwest Pacific warming and southward migration of the ITCZ reduce the strength of the off-equatorial heat source and thus weaken the equatorial westerly wind anomalies (Figs. 3c,d). Again, anomalous warming in the western Pacific relative to the eastern Pacific generates a negative east–west SSTA gradient that intensifies the easterlies over the central equatorial Pacific and further damps equatorial warming (Figs. 3c,d). By winter, the surface warming disappears almost completely (Fig. 3d). The lack of sufficient positive subsurface anomalies for most of the +SFM simulation

Brought to you by NOAA Central Library | Unauthenticated | Downloaded 10/12/21 03:47 PM UTC

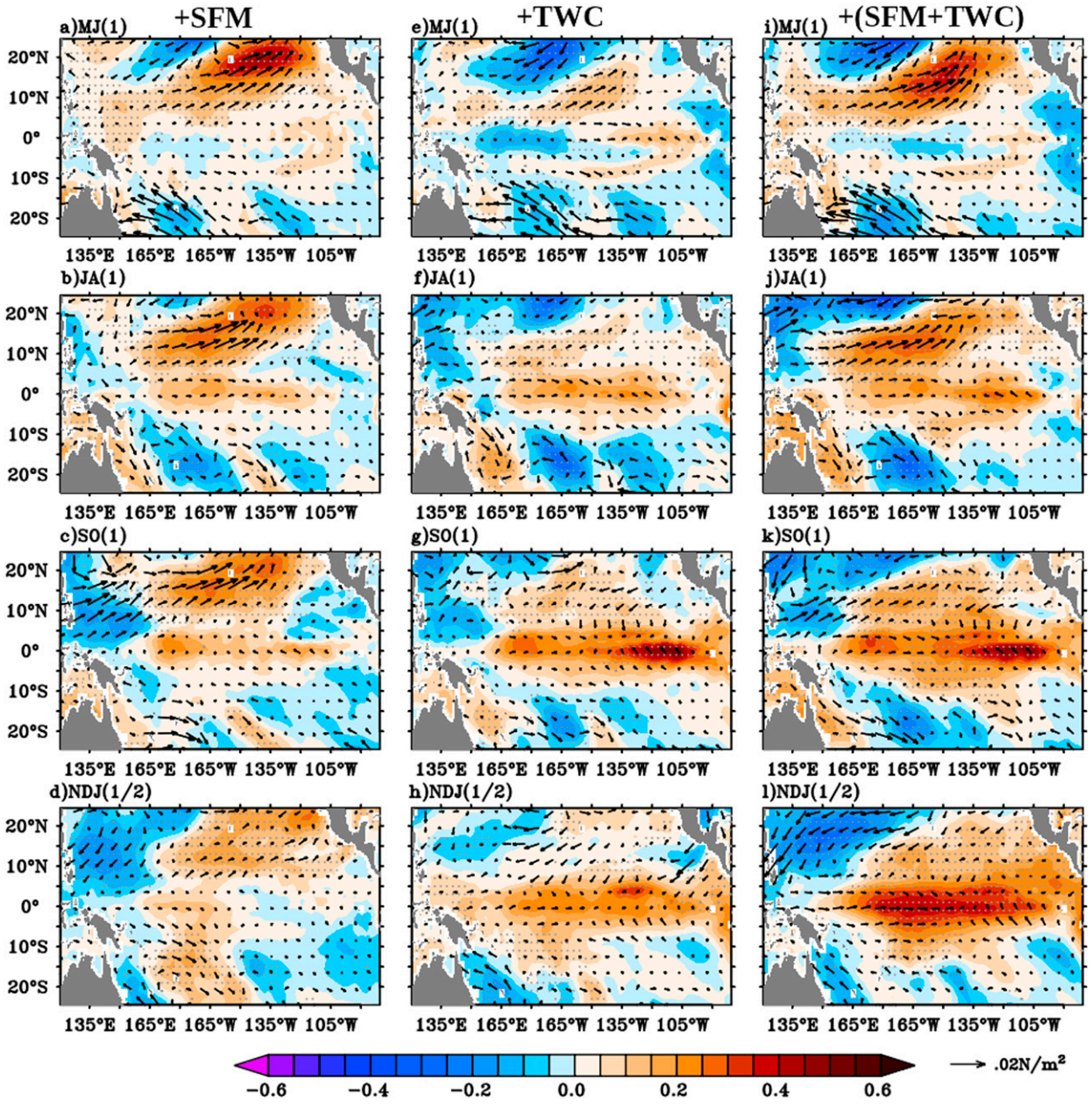

FIG. 3. Ensemble mean model response of SST (°C; shading), wind stress, and tau (N m^{-2}; vectors) scaled to the reference vector in the bottom-right corner: (a)–(d) +SFM net heat flux forcing, (e)–(h) +TWC wind stress forcing, and (i)–(l) combined +(SFM + TWC) forcing during the coupled stage in (top) May–June year 1 [MJ(1)], (top middle) July–August year 1 [JA(1)], (bottom middle) September–October year 1 [SO(1)], and (bottom) November–December year 1 and January year 2 [NDJ(1/2)]. Stippling indicates regions where the ensemble mean differences are significant with 90% confidence from a two-tailed Student's *t* test.

(Figs. 4a–d) reflects the absence of a charged equatorial Pacific that hinders the amplification of El Niño. Thus, the +SFM forcing generates a weak, short-lived CP El Niño–like warming in the fall.

For the +TWC experiment, weak wind anomalies occur over the equatorial Pacific in early summer of year 1 (Fig. 3e). In the east, however, SST anomalies begin to increase due to the seasonal upwelling of anomalously warm subsurface water, which has accumulated in response to the +TWC forcing during spring (Fig. 2f) and then eventually advected eastward and upward along the tilted equatorial thermocline (Figs. 4e–g). The upwelling of warm water erodes the cold springtime anomalies in the eastern equatorial Pacific (Fig. 2b) and initiates surface warming (Fig. 3e). This warming allows the Bjerknes feedback (Bjerknes 1969) to operate and generate westerly wind anomalies in the central equatorial Pacific in late summer (Fig. 3f). These westerly

Brought to you by NOAA Central Library | Unauthenticated | Downloaded 10/12/21 03:47 PM UTC

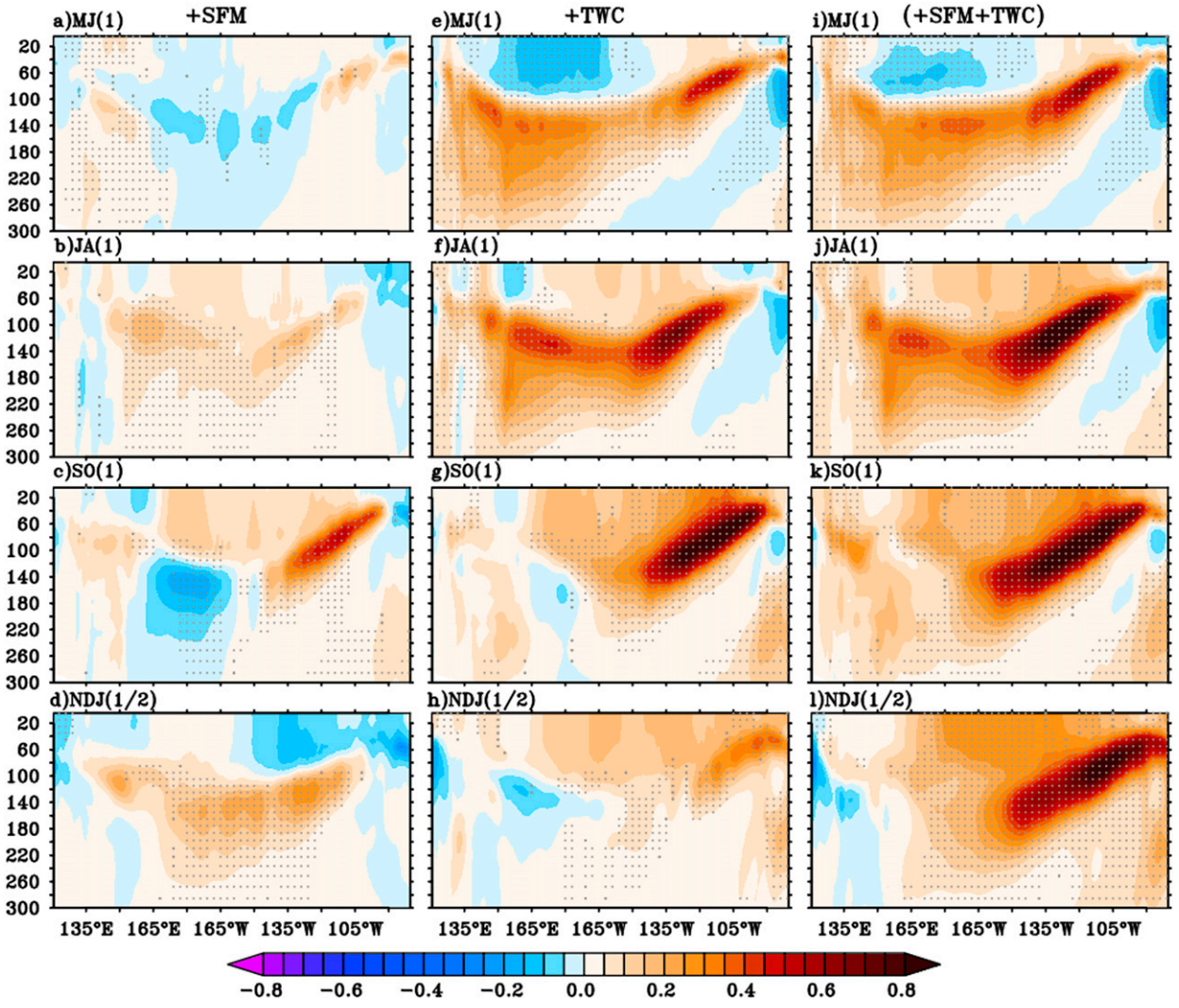

FIG. 4. As in Fig. 3, but meridionally averaged (3°N–3°S) temperature anomalies for the (a)–(d) +SFM, (e)–(h) +TWC, and (i)–(l) +(SFM + TWC) ensemble response. Stippling indicates regions where the ensemble mean differences are significant with 90% confidence from a two-tailed Student's *t* test.

anomalies reduce equatorial upwelling and allow the surface waters to continue to warm such that, during fall of year 1, a moderate (~0.5°C) EP El Niño–like warming (Anderson and Perez 2015) develops (Fig. 3g) that persists until winter (Fig. 3h).

In the +(SFM + TWC) experiment during early summer of year 1, the off-equatorial surface warming is stronger and stretches farther equatorward in the central Pacific (Fig. 3i) relative to the +SFM experiment (Fig. 3a). This combined +SFM and +TWC forcing generates stronger southwesterly wind anomalies north of the equator and, through WES feedback, generates stronger SSTAs in the northwest Pacific (Fig. 3i). In late summer of year 1, the resultant off-equatorial heat source produces stronger westerly anomalies relative to when only +SFM forcing is applied, producing stronger western equatorial Pacific warming (Fig. 3j). At the same time, seasonal upwelling in the east brings anomalously warm subsurface waters to the surface (Fig. 4j) and generates local surface warming in the eastern Pacific (Fig. 3j), which drives westerly wind anomalies over the western and central equatorial Pacific. Together these factors intensify the westerly anomalies across the equatorial Pacific. Further, the subsurface warming (i.e., charging) is stronger in the +(SFM + TWC) experiment throughout the coupled stage (Figs. 4i–l) than in the +TWC experiment. As a result, the combined effect of +(SFM+TWC) forcing produces a stronger El Niño response (~0.6°C) in the winter relative to the +SFM and +TWC experiments (cf. Fig. 3l with Fig. 3c and Fig. 3h, respectively).

c. *Time evolution of equatorial Pacific in the ensemble experiment*

In Fig. 5 we compare the time evolution of equatorial Pacific SST and SSH anomalies for the three experiments. For the +SFM experiment, the net heat flux forcing imposed over

Brought to you by NOAA Central Library | Unauthenticated | Downloaded 10/12/21 03:47 PM UTC

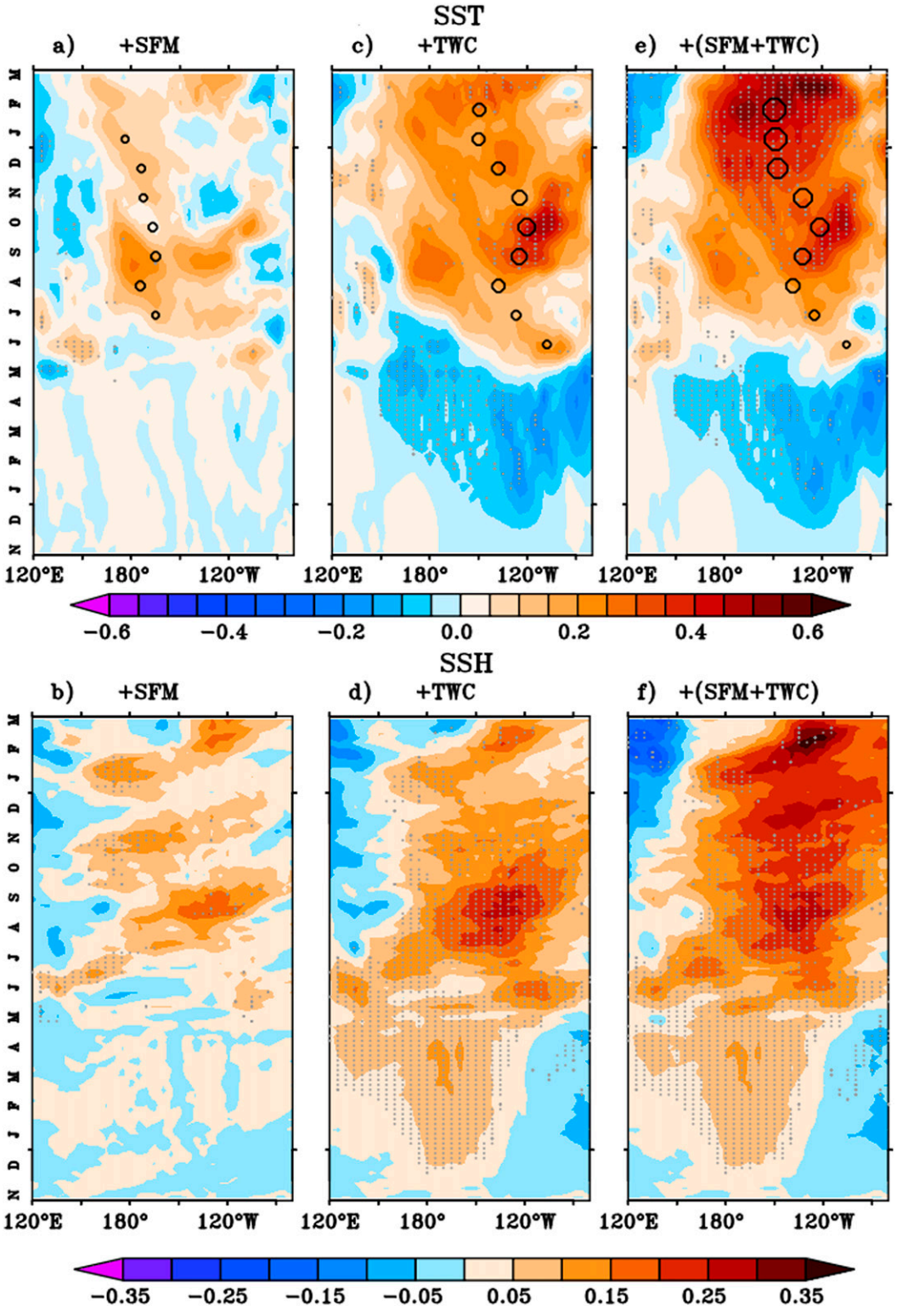

FIG. 5. Time–longitude plots of the (a),(b) +SFM ensemble response, (c),(d) +TWC ensemble response, and (e),(f) +(SFM + TWC) ensemble response of (top) SST (°C) and (bottom) SSH (m) anomalies (difference between +TWC and no trade-wind charging, CLIM, ensemble mean) along the equator (meridionally averaged from 3°S to 3°N) from November of year 0 to March of year 2. Areas are stippled where values exceed the 90% confidence level from a two-tailed Student's *t* test. The position and size of black circles in (a), (c), and (e) show the location and magnitude, respectively, of location (longitude) of the center of heat anomaly for each month. The smallest circle corresponds to a +0.1°C center of heat anomaly, and the largest circle corresponds to a +0.5°C anomaly.

Brought to you by NOAA Central Library | Unauthenticated | Downloaded 10/12/21 03:47 PM UTC

the off-equatorial North Pacific during the forced stage has no significant impact on the equatorial Pacific SST (Fig. 5a) or SSH (Fig. 5b) anomalies. After coupling is engaged, air–sea interactions induce zonal wind stress anomalies over the western equatorial Pacific (not shown). In June of year 1, anomalous westerlies trigger an eastward propagating downwelling Kelvin wave, evident as a positive SSHA that transits the basin from June to September (Fig. 5b). This generates positive SSTAs (Fig. 5a) across the central equatorial Pacific (center of heat near 170°W; black circles in Fig. 5a) and the formation of CP El Niño–like warming with a peak amplitude of 0.25°C in August–September that begins to decay in October.

In contrast, the +TWC forced experiment initially has cold SST anomalies (Fig. 5c), suggestive of La Niña–like conditions. However, the gradual increase in positive SSHA over the central equatorial Pacific from December of year 0 onward (Fig. 5d) indicates a steady buildup of subsurface heat content. The subsurface heat advects eastward, eventually initiating eastern Pacific SST warming in May of year 1 (Figs. 5c,d). This warming initiates the Bjerknes feedback (Bjerknes 1969) by generating westerly anomalies (Figs. 3e,f) that further intensify the equatorial warming mainly in the eastern Pacific, leading to the development of a mature EP-like El Niño (Fig. 5c). Interestingly, it appears that a second pulse of subsurface heat content anomalies, initially found in the far western Pacific in June of year 1, also advects eastward, augmenting the east subsurface anomalies that were already developing (Figs. 5c,d). This secondary subsurface anomaly depicts the western boundary reflection of westward propagating Rossby waves that developed (Alexander et al. 2010; Chakravorty et al. 2020) during previous winter and spring (Fig. 2e). The +TWC ensemble generates an EP-like El Niño with the center of heat near 120°W in fall (Fig. 5c) that persists until late winter of year 1 (when the center of heat in winter shifts to 140°W).

For the +(SFM + TWC) experiment, the equatorial evolution is nearly identical to the +TWC until April of year 1; at this time, the introduction of air–sea coupling drives a stronger basinwide warming in the spring and winter in the +(SFM + TWC) experiment (Fig. 5e). The similarity between the +(SFM + TWC) and +TWC experiments in the initial surface and subsurface response suggests that the generation of warm anomalies is primarily due to the TWC mechanism. However, the combined forcing produces a stronger westerly wind anomaly (Fig. 3j) than the +TWC experiment (Fig. 3f), driving more pronounced SST and SSH anomalies via coupled air–sea processes. We hypothesize that the stronger, more persistent subsurface warming in +(SFM + TWC) (see below) drives the stronger and more widespread El Niño conditions centered near 140°W in winter of year 1 as compared with the generally weaker conditions in +TWC (Figs. 5e,f).

d. Mixed layer heat budget

Next, we performed a mixed layer heat budget analysis to better understand the physical processes responsible for the equatorial Pacific SST response within the different experiments (Fig. 6). To do so, the equation (Kug et al. 2009; Montégut et al. 2007) applied to the ensemble experiments is as follows:

$$\frac{\partial T}{\partial t} = \frac{Q_s}{\rho C_P h} - \frac{1}{h}\int\left(u\frac{\partial T}{\partial x} + v\frac{\partial T}{\partial y}\right)dz - \frac{1}{h}(T - T_h)\left(W_h + \frac{\partial h}{\partial t}\right) - \frac{1}{h}\left(K_z\frac{\partial T}{\partial z}\right)_h + R,$$

where T is the mixed layer temperature; h is the depth of the mixed layer; (u, v) are horizontal velocity; T_h and W_h are the temperature and vertical velocity at the base of the mixed layer, respectively; Q_S is net heat flux at the sea surface; ρ is the seawater reference density; C_P is the specific heat capacity of seawater; and K_z is the vertical mixing coefficient. The residual term R is small in the ensemble mean (Montégut et al. 2007). The major processes that determine the mixed-layer temperature tendency (TEND; term on the left-hand side) in the equatorial Pacific include (i) surface net heat flux [NHF; first term on the right-hand side (RHS)], (ii) horizontal advection (HADV; second term on the RHS), and (iii) vertical oceanic subsurface processes (VSUB; third and fourth terms on the RHS), including vertical advection, entrainment mixing, and diffusion. For each simulation we computed each heat budget term for a given ensemble run and experiment and then calculated the ensemble mean anomalies for each experiment with respect to the CLIM ensemble mean. We then applied a 45-day low-pass filter and averaged over 2°S–2°N. Note that the depth of the mixed layer h is temporally and geographically varying and is defined as the depth at which the potential density difference exceeds 0.01 kg m^{-3}.

In the +SFM experiment, as expected, the tendency term is negligible until spring over the equatorial Pacific (Fig. 6a). Starting in early summer of year 1, a significant warming tendency begins near 150°W (Fig. 6a), resulting primarily from anomalous horizontal advection of warm water (Fig. 6c) due to the anomalous equatorial westerly wind. However, in late fall and winter (of year 1), as the westerly anomalies decay and easterly trades strengthen over the central equatorial Pacific (Figs. 3c,d), anomalous horizontal advection allows cold water to advect into the central equatorial Pacific and leads to the decay of the positive surface temperature anomalies. Oceanic vertical processes have a fairly small contribution to the warming for most of the experiment (Fig. 6d). Instead, the generation and decay of the warm event is primarily driven by zonal advection (Fig. 6c), consistent with previous CP El Niño studies (Kug et al. 2009).

Turning to the +TWC experiment, the initial cooling tendency (Fig. 6e) is associated with vertical processes in the eastern Pacific (Fig. 6h) and horizontal advection in the western and central Pacific (Fig. 6g). In summer of year 1, a shift to a warming tendency in the east Pacific (Fig. 6e) is initiated by oceanic vertical processes (Fig. 6h), primarily due to the mean upwelling of anomalously warm subsurface water [thermocline feedback term $\overline{W}(\delta T/\delta t)$; not shown] rather than the upwelling feedback term $W(\delta\overline{T}/\delta t)$. These vertical advection processes are eventually supported by the zonal advection term. The resulting warming sets up westerly wind anomalies in the central Pacific (i.e., the Bjerknes feedback; Bjerknes 1969) that

Brought to you by NOAA Central Library | Unauthenticated | Downloaded 10/12/21 03:47 PM UTC

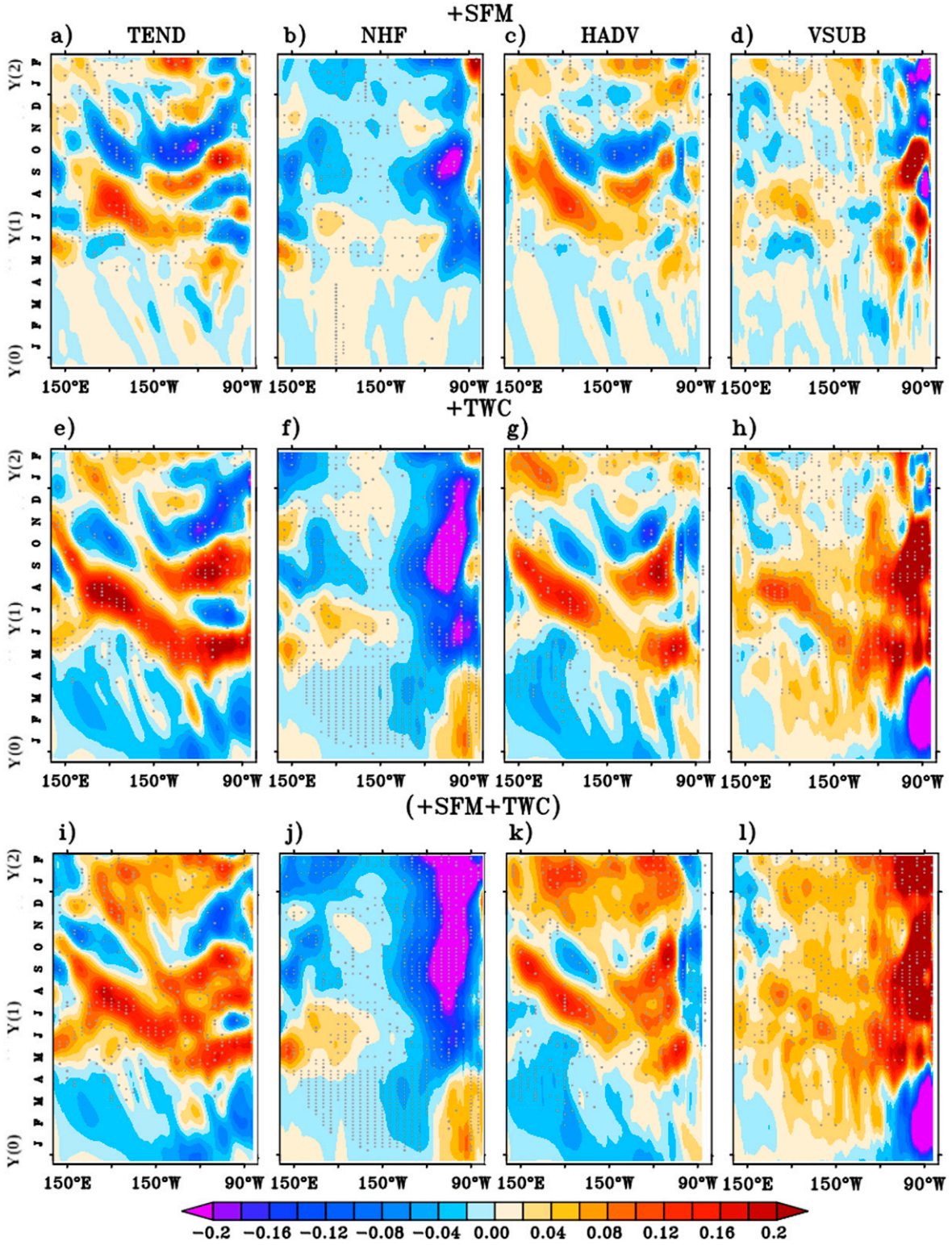

FIG. 6. Time–longitude plots of the (a)–(d) +SFM ensemble mean response, (e)–(h) +TWC ensemble response, and (i)–(l) +(SFM + TWC) response of (left) mixed layer temperature tendency (Tm_tend; °C month^{-1}), (center left) net heat contribution (Q; °C month^{-1}), (center right) horizontal advection (HADV; °C month^{-1}), and (right) the vertical oceanic subsurface processes (VSUB; °C month^{-1}) along the equator (meridionally averaged from 2°S to 2°N). Stippling indicates regions where the ensemble mean differences are significant with 90% confidence from a two-tailed Student's t test.

Brought to you by NOAA Central Library | Unauthenticated | Downloaded 10/12/21 03:47 PM UTC

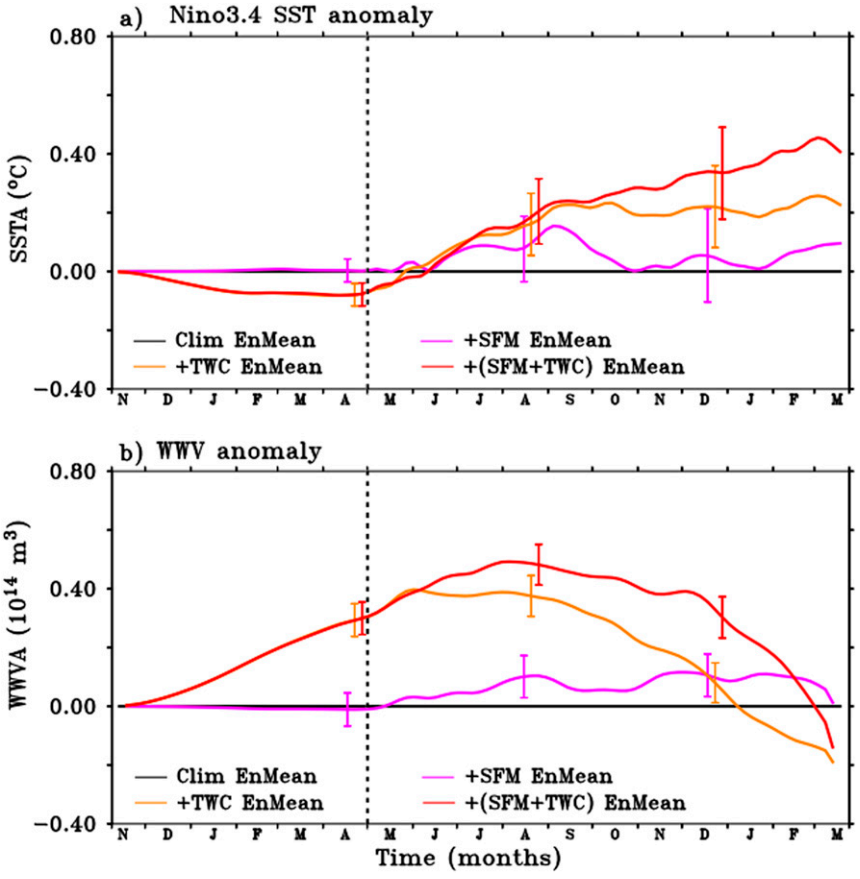

FIG. 7. Evolution of 5-day ensemble mean anomalies of (a) Niño-3.4 SST (°C) with 45-day smoothing from November of year 0 to March of year 2 for the +SFM ensemble mean (pink lines), +TWC ensemble mean (orange lines), and +(SFM + TWC) ensemble mean (red lines); (b) as in (a), but for warm water volume (WWV; 10^{14} m^3) averaged from 120°E to 80°W and from 5°N to 5°S. The vertical lines show the spread (standard error) of the respective simulation about its mean for April of year 1, August of year 1, and November–December of year 1 and January of year 2. The black vertical dashed lines indicate the start of the fully coupled stage.

intensify the warming and spread it westward through horizontal advection and vertical processes from summer to early winter of year 1 (Figs. 6g,h). Countering these heating processes is a strong negative NHF in the eastern Pacific (Fig. 6f) that acts to dampen the El Niño warming. Interestingly, the horizontal advection of warm water is stronger in the +TWC experiment than the +SFM. That said, the thermocline feedback (due to warm subsurface temperature) is the dominant term in the +TWC experiment evolution, which is subsequently augmented by horizontal advection (due to strong and persistent westerly wind stress anomalies). As Xie and Jin (2018) note, the thermocline feedback process plays a crucial role in generating EP El Niño–type warming, consistent with the El Niño evolution and positioning seen in the +TWC experiments.

The +(SFM + TWC) experiment initially follows a similar evolution as the +TWC experiment (Figs. 6e,i). However, the warming tendency persists longer (Fig. 6i) due to a continued supply of warm water by oceanic vertical processes and horizontal advection (Figs. 6k,l) that overwhelms the increased negative NHF term (Fig. 6j) and acts to sustain the equatorial Pacific warming.

e. *Ensemble mean and spread*

We quantitatively compare the ensemble mean and spread of Niño-3.4 SST and warm water volume (WWV; Meinen 2000) anomalies for the experiments (Fig. 7). The ensemble mean Niño-3.4 SST anomalies are near-zero for +SFM until April of year 1 (pink lines in Fig. 7a), and for both +TWC and +(SFM + TWC) they are weakly negative, with very small ensemble spread (orange and red lines, respectively, in Fig. 7a). With air–sea coupling, ensembles of each experiment begin to diverge in the summer with increased ensemble spread (Fig. 7a). Throughout the +SFM experiment, Niño-3.4 anomalies are never significantly different from zero, but the +TWC and +(SFM + TWC) experiments show significant winter warming in year 1.

In contrast, the WWV evolution for the +TWC and +(SFM + TWC) experiments quickly increases in response to warm water charging, which diverges from the near-zero WWV anomaly observed in the +SFM experiment (Fig. 7b). As with the Niño-3.4

Brought to you by NOAA Central Library | Unauthenticated | Downloaded 10/12/21 03:47 PM UTC

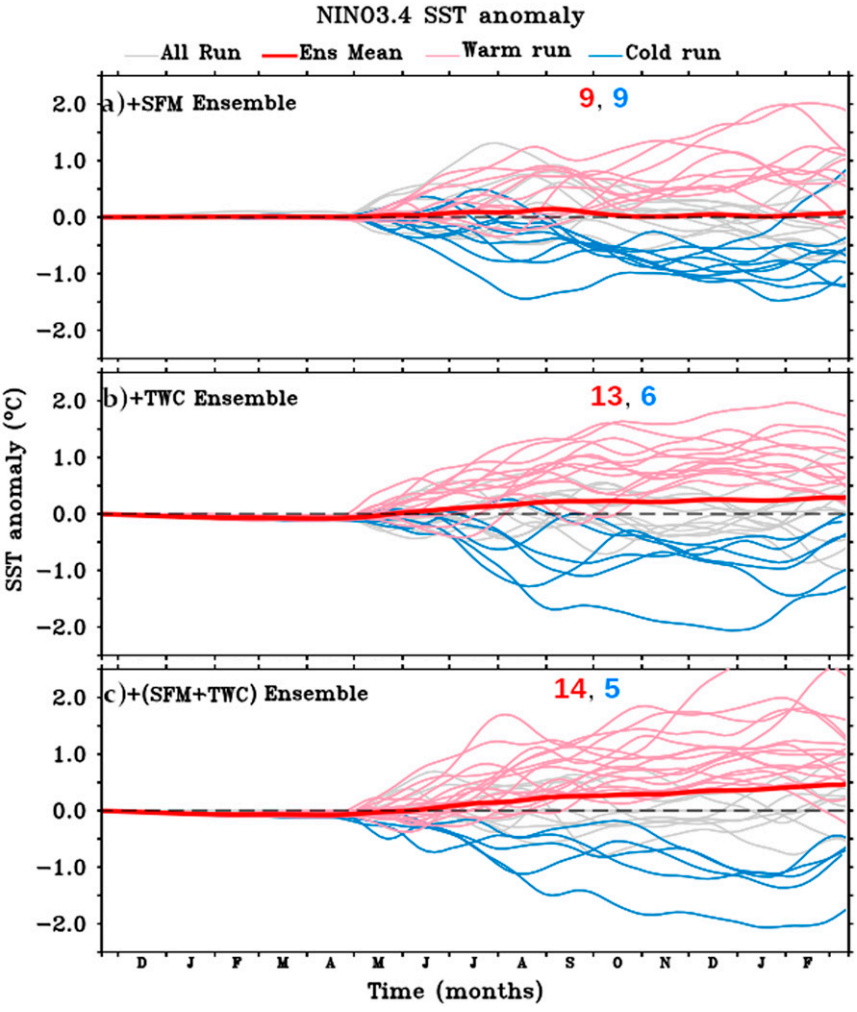

FIG. 8. Five-day mean (a) Niño-3.4 SST (°C) anomalies with 45-day smoothing for the 30 (a) +SFM, (b) +TWC, and (c) +(SFM + TWC) ensembles computed by removing the corresponding CLIM ensemble member. The thin red lines indicate ensembles warmer than 0.5°C (warm ensembles), thin blue lines indicate ensembles cooler than −0.5°C (cold ensembles), and gray lines indicate ensembles between −0.5°C and 0.5°C (neutral ensembles) during NDJ(1/2).

SSTAs, the ensemble mean WWV anomalies for the +(SFM + TWC) overlap with the +TWC until summer of year 1. However, the accumulation of warm water over the equatorial Pacific becomes significantly larger in the +(SFM + TWC) relative to the +TWC experiment in the fall. By the end of the +TWC and +(SFM + TWC) experiments in spring of year 2, negative WWV anomalies develop, consistent with the expected poleward warm water discharge during the peak phase of El Niño (Jin 1997).

To check the robustness of these ENSO responses, we examined the time evolution of Niño-3.4 SSTAs for the 30 ensemble members (each calculated with respect to the corresponding CLIM ensemble member). In the presence of coupling, the Niño-3.4 SSTAs for the 30 ensemble members quickly diverge in all three experiments (Fig. 8). This initial spread is most likely due to stochastic atmospheric variability occurring shortly after the introduction of coupling, as demonstrated in Larson and Kirtman (2017). Despite this large spread, we find that in the +SFM experiment (Fig. 8a) during NDJ(1/2), the warm (>0.5°C) and cold (<0.5°C) ensembles are evenly distributed with 9 warm and 9 cold ensembles. In contrast, there are more than 2 times as many warm versus cold ensemble members (13 warm and 6 cold ensembles; Fig. 8b) in the +TWC experiment. Under combined forcing, the number of warm ensemble members increases to nearly triple the number of cold ensemble members (14 warm and 5 cold events; Fig. 8c). Although not shown here, when compared with the CLIM ensemble mean (rather than individual CLIM ensemble members) Niño-3.4 SSTAs, all three experiments result in similar overall numbers of warm (>0.5°C) events (12–13 events, as compared with the 7 events in the CLIM). However, only 15% of the +SFM warm events constitute strong events (>1°C, which represents the 90% threshold from the CLIM experiment, i.e., only occurs 10% of the time), whereas 50% and 75% of the +TWC and +(SFM + TWC) warm events exceed this threshold, respectively.

Brought to you by NOAA Central Library | Unauthenticated | Downloaded 10/12/21 03:47 PM UTC

As Niño-3.4 SSTAs are computed over a fixed domain, this may not be the best index to capture the different spatial flavor of the El Niño events that develop. Thus, we further analyze the longitudinal location of the center of peak surface warming (meridionally averaged SSTAs from 3°S to 3°N) for each of the ensemble members relative to the CLIM ensemble mean (not shown). We examine the longitudes of peak warming (similar to what was done for the ensemble means, i.e., the black circles in Fig. 5) only for those ensemble members for which the SSTAs exceed 0.5°C in NDJ(1/2) along the equatorial Pacific. We find that 75% of +SFM warm ensembles (9 of the 12 ensembles) exhibited CP El Niño–like warming (center of heat located west of 150°W) in winter. In contrast, in the +TWC experiment 70% of the warm ensemble (10 of the 14 ensembles) show EP El Niño–like characteristics (center of heat located east of 150°W). When combined in the +(SFM + TWC) experiment, most of the warm ensembles begin with east Pacific warming, but in the winter the center of peak warming is located around 150°W for 70% of warm ensembles (11 of 16 warm ensembles). This suggests that the subsurface warm water recharge associated with the +TWC mechanism favors the formation of eastern Pacific warming events, whereas the addition of +SFM shifts the warming westward.

4. Summary and discussion

Our study highlights the importance of extratropical Pacific atmospheric forcing on El Niño generation, focusing on two key mechanisms, the heat flux–driven SFM and ocean dynamics–driven TWC mechanism. Through these two mechanisms, the extratropics can influence El Niño events up to a year in advance. Our findings suggest that the +SFM, through thermodynamically coupled processes, produces an off-equatorial heat source (e.g., Amaya et al. 2019; Vimont et al. 2003) that drives equatorial westerly wind anomalies and generates a weak, short-lived CP El Niño–like warming pattern in the fall. In these runs, the warming decays quickly as the western Pacific warming reinforces the east–west SST gradient and easterly trade winds in fall and winter, which advect cold water into the central equatorial Pacific in the absence of strong subsurface warming. On the other hand, +TWC, through ocean dynamical processes, successfully charges the central equatorial Pacific with warm water (e.g., Anderson 2007; Anderson and Perez 2015; Chakravorty et al. 2020). This warm water subsequently advects eastward and upward along the tilted thermocline and generates a moderate EP El Niño–like warm event (Chakravorty et al. 2020). When both mechanisms occur in tandem, they generate a stronger and more persistent El Niño with basinwide warming, initiated primarily by the +TWC mechanism but augmented by the +SFM. This comparative analysis of dynamical and thermodynamical mechanisms suggests that while an El Niño can be triggered by both dynamic and thermodynamic processes, its strength, growth, and persistence depends largely on the dynamically driven subsurface ocean response. The distinctly different longitudinal position of warming over the equatorial Pacific by these two mechanisms further suggests that extratropical forcing can influence ENSO diversity [consistent with previous studies including Yu and Kim (2010, 2011), Yu et al. (2017), and Pegion et al. (2020)]. In our experiments, heat flux–driven processes alone tend to generate central Pacific warming, whereas a charged equatorial Pacific preconditioning favors eastern Pacific warming.

Given these results, it is interesting to note that X. Wang et al. (2019) found that coupled models that are significantly better in representing the surface air–sea thermodynamic coupling associated with NPO are better in simulating central Pacific El Niño events. Further, the inability of coupled models to properly simulate extratropical Pacific modes such as the NPO (Lin et al. 2015) may contribute to their limited ENSO predictability (Fedorov et al. 2003, Wang et al. 2021). As such, our results highlight the need for proper representation of extratropical mechanisms in coupled models, as these mechanisms influence the magnitude and structure of ENSO events and could contribute to improved ENSO predictability. We note that our results are not necessarily analogous for how extratropical forcing from the Southern Hemisphere may influence ENSO diversity. For example, Larson et al. (2018b) show that thermodynamically driven variability from the southeast Pacific more directly impacts east Pacific SSTA through modulation of the overlying latent heat fluxes, rather than central Pacific SSTA. It also is important to note that our experiments are initialized from nearly neutral conditions, and as such do not include interactions between ocean preconditioning and the +SFM or +TWC mechanisms. Studies show that ocean preconditioning associated with the traditional Jin (1997) recharge/discharge can explain 30% of ENSO variability in coupled model experiments (Larson and Kirtman 2017). A recent study by Santoso et al. (2017) also found that a positive NPMM superimposed on strong ocean preconditioning may be what lead to the extreme 2015/16 El Niño event. Thus, the interaction between extratropical forcing and ocean preconditioning in the tropical Pacific Ocean is an important area of study that will be explored in future research.

Acknowledgments. This work was supported by National Science Foundation (NSF) Grants AGS-1547137 (authors Chakravorty and Perez), AGS-1547412 (authors Anderson and Pivotti), and AGS-1547398 (author Giese). Chakravorty and Perez acknowledge support from NOAA's Atlantic Oceanographic and Meteorological Laboratory. Chakravorty was supported under the auspices of the Cooperative Institute for Marine and Atmospheric Studies (CIMAS), a cooperative institute of the University of Miami and NOAA, under cooperative agreement NA20OAR4320472. Author Larson acknowledges support from NSF Grant AGS-1951713. We also acknowledge the high-performance computing support from Cheyenne (https://doi.org/10.5065/D6RX99HX) provided by NCAR's Computational and Information Systems Laboratory, sponsored by NSF. We also thank Dr. Dongmin Kim, Dr. Libby Johns, Ms. Gail Derr, and the three anonymous reviewers and the journal editor for their helpful comments and suggestions.

APPENDIX

Method to Generate TWC and SFM Forcing

To identify TWC-related wind stress fields and SFM-related net heat flux from within the SODAsi.3 reanalysis product we

Brought to you by NOAA Central Library | Unauthenticated | Downloaded 10/12/21 03:47 PM UTC

first isolate the mode of tropical boreal winter horizontal wind stress that 1) has the highest correlation with tropical SST variability during the following boreal winter and 2) is independent from the concurrent ENSO state. To do so, we use monthly SST and zonal wind stress τ_x from the SODAsi.3 and 20CRv2c dataset respectively. These first steps are nearly identical to the process outlined in Chakravorty et al. (2020).

The fields of SST and τ_x are constrained to the region between latitudes 20°S and 20°N and longitudes 120°E and 70°W. Furthermore, because the modes we are interested in are most active during boreal winter, the variables are seasonally averaged from November to January for SST (Trenberth 1997) and from November to February for τ_x and the seasonal means are linearly detrended across all years (Anderson and Perez 2015). To further improve robustness of the results, the data processing described above is run identically on the last 60 years (1952–2011) of all eight ensemble members ($60 \times 8 = 480$ years) available from the two reanalysis products [as described in Chakravorty et al. (2020)].

Having obtained the spatiotemporal evolution of boreal winter, tropical Pacific τ_x and SST anomalies, we next seek to identify modes of τ_x variability that precede large-scale changes in the boreal winter SST structure the following year by adopting a variant of the canonical correlation analysis (CCA) used by Anderson (2003). As in previous analyses (e.g., Bretherton et al. 1992; Graham et al. 1987) we first isolate large-scale modes of variability in both fields by separately applying EOF analysis and then, following the method outlined by Anderson (2003) and Chakravorty et al. (2020), we include their respective leading EOF time series in the CCA. The subsets, specifically, include the first 10 modes for SST and the first 9 modes for the wind stress. To avoid the influence of concurrent, ENSO-related wind stress anomalies, we remove these anomalies by excluding from the CCA the first EOF of τ_x, which captures the time evolution of ENSO-related wind stress anomalies (Chakravorty et al. 2020; Larson and Kirtman 2014). The CCA analysis returns pairs of time series, called canonical variables (CV), one for SST and one for τ_x, among which the first one is the one carrying the highest correlation value. We then use the first CV of τ_x to reconstruct both TWC and SFM fields applying a weighted composite algorithm to the anomaly fields of wind stress (τ_x and τ_y) and net heat flux Q_n, respectively. As one can see from Fig. 1d the net heat flux has been masked near the equator. This choice was made to exclude those values for which the concurrent SST and Q_n anomalies have opposite signs.

Selection of ENSO-neutral initial condition

For our ensemble experiment we select the 1 November initial conditions from the control simulation that 1) are in an ENSO-neutral equatorial Pacific state at the onset of the experiment and 2) have a tendency to remain ENSO-neutral over the course of the following winter by applying the two following criteria [as in Chakravorty et al. (2020)]. First, the monthly averaged Niño-3.4 SST anomalies (relative to the climatological mean of the 222-yr coupled simulation) on 1 November of year 0 must be within the range of ±0.5°C (to ensure that near-neutral conditions exist in the equatorial Pacific SST). Second, the Niño-3.4 SST anomaly one year later, during the subsequent winter November and December of year 1 and January of year 2, NDJ(1/2), must be within the range of ±1°C (to ensure the absence of any subsurface precursor conditions in the initial ocean state that could result in the development of a mature ENSO event the following year). A total of 30 branch points are selected as initial conditions for the ensemble experiments.

REFERENCES

Alexander, M. A., D. J. Vimont, P. Chang, and J. D. Scott, 2010: The impact of extratropical atmospheric variability on ENSO: Testing the seasonal footprinting mechanism using coupled model experiments. *J. Climate*, **23**, 2885–2901, https://doi.org/10.1175/2010JCLI3205.1.

Amaya, D. J., Y. Kosaka, W. Zhou, Y. Zhang, S.-P. Xie, and A. J. Miller, 2019: The North Pacific pacemaker effect on historical ENSO and its mechanisms. *J. Climate*, **32**, 7643–7661, https://doi.org/10.1175/JCLI-D-19-0040.1.

Anderson, B. T., 2003: Tropical Pacific sea-surface temperatures and preceding sea-level pressure anomalies in the subtropical North Pacific. *J. Geophys. Res.*, **108**, 4732, https://doi.org/10.1029/2003JD003805.

——, 2007: On the joint role of subtropical atmospheric variability and equatorial subsurface heat content anomalies in initiating the onset of ENSO events. *J. Climate*, **20**, 1593–1599, https://doi.org/10.1175/JCLI4075.1.

——, and R. C. Perez, 2015: ENSO and non-ENSO induced charging and discharging of the equatorial Pacific. *Climate Dyn.*, **45**, 2309–2327, https://doi.org/10.1007/s00382-015-2472-x.

——, ——, and A. Karspeck, 2013: Triggering of El Niño onset through trade wind–induced charging of the equatorial Pacific. *Geophys. Res. Lett.*, **40**, 1212–1216, https://doi.org/10.1002/grl.50200.

Ashok, K., S. K. Behera, S. A. Rao, H. Y. Weng, and T. Yamagata, 2007: El Niño Modoki and its possible teleconnection. *J. Geophys. Res. Oceans*, **112**, C11007, https://doi.org/10.1029/2006JC003798.

Battisti, D. S., and A. C. Hirst, 1989: Interannual variability in a tropical atmosphere–ocean model: Influence of the basic state, ocean geometry and nonlinearity. *J. Atmos. Sci.*, **46**, 1687–1712, https://doi.org/10.1175/1520-0469(1989)046<1687:IVIATA>2.0.CO;2.

Bjerknes, J., 1969: Atmospheric teleconnections from the equatorial Pacific. *Mon. Wea. Rev.*, **97**, 163–172, https://doi.org/10.1175/1520-0493(1969)097<0163:ATFTEP>2.3.CO;2.

Bretherton, C. S., C. Smith, and J. M. Wallace., 1992: An intercomparison of methods for finding coupled patterns in climate data. *J. Climate*, **5**, 541–560, https://doi.org/10.1175/1520-0442(1992)005<0541:AIOMFF>2.0.CO;2.

Cane, M. A., and S. E. Zebiak, 1985: A theory for El Niño and the Southern Oscillation. *Science*, **228**, 1085–1087, https://doi.org/10.1126/science.228.4703.1085.

Capotondi, A., and Coauthors, 2015: Understanding ENSO diversity. *Bull. Amer. Meteor. Soc.*, **96**, 921–938, https://doi.org/10.1175/BAMS-D-13-00117.1.

Carton, J. A., and B. S. Giese, 2008: A reanalysis of ocean climate using Simple Ocean Data Assimilation (SODA). *Mon. Wea. Rev.*, **136**, 2999–3017, https://doi.org/10.1175/2007MWR1978.1.

Chakravorty, S., J. S. Chowdary, and C. Gnanaseelan, 2013: Spring asymmetric mode in the tropical Indian Ocean: Role of El Niño and IOD. *Climate Dyn.*, **40**, 1467–1481, https://doi.org/10.1007/s00382-012-1340-1.

Brought to you by NOAA Central Library | Unauthenticated | Downloaded 10/12/21 03:47 PM UTC

——, C. Gnanaseelan, and P. A. Pillai, 2016: Combined influence of remote and local SST forcing on Indian summer monsoon rainfall variability. *Climate Dyn.*, **47**, 2817–2831, https://doi.org/10.1007/s00382-016-2999-5.

——, R. C. Perez, B. T. Anderson, B. S. Giese, S. M. Larson, and V. Pivotti, 2020: Testing the trade wind charging mechanism and its influence on ENSO variability. *J. Climate*, **33**, 7391–7411, https://doi.org/10.1175/JCLI-D-19-0727.1.

Chiang, J. C. H., and D. J. Vimont, 2004: Analogous Pacific and Atlantic meridional modes of tropical atmosphere–ocean variability. *J. Climate*, **17**, 4143–4158, https://doi.org/10.1175/JCLI4953.1.

Clarke, A. J., S. Van Gorder, and G. Colantuono, 2007: Wind stress curl and ENSO discharge/recharge in the equatorial Pacific. *J. Phys. Oceanogr.*, **37**, 1077–1091, https://doi.org/10.1175/JPO3035.1.

Fedorov, A. V., S. L. Harper, S. G. Philander, B. Winter, and A. Wittenberg, 2003: How predictable is El Niño? *Bull. Amer. Meteor. Soc.*, **84**, 911–920, https://doi.org/10.1175/BAMS-84-7-911.

Gettelman, A., and Coauthors, 2010: Global simulations of ice nucleation and ice supersaturation with an improved cloud scheme in the Community Atmosphere Model. *J. Geophys. Res.*, **115**, D18216, https://doi.org/10.1029/2009JD013797.

Giese, B. S., H. F. Seidel, G. P. Compo, and P. D. Sardeshmukh, 2016: An ensemble of ocean reanalyses for 1815–2013 with sparse observational input. *J. Geophys. Res. Oceans*, **121**, 6891–6910, https://doi.org/10.1002/2016JC012079.

Gill, A. E., 1980: Some simple solutions for heat-induced tropical circulation. *Quart. J. Roy. Meteor. Soc.*, **106**, 447–462, https://doi.org/10.1002/qj.49710644905.

Graham, N. E., J. Michaelsen, and T. P. Barnett, 1987: An investigation of the El Niño–Southern Oscillation cycle with statistical models: 1. Predictor field characteristics. *J. Geophys. Res.*, **92**, 14 251–14 270, https://doi.org/10.1029/JC092iC13p14251.

Hurrell, J. W., and Coauthors, 2013: The Community Earth System Model: A framework for collaborative research. *Bull. Amer. Meteor. Soc.*, **94**, 1339–1360, https://doi.org/10.1175/BAMS-D-12-00121.1.

Ineson, S., and Coauthors, 2018: Predicting El Niño in 2014 and 2015. *Sci. Rep.*, **8**, 10733, https://doi.org/10.1038/s41598-018-29130-1.

Infanti, J. M., and B. P. Kirtman, 2016: North American rainfall and temperature prediction response to the diversity of ENSO. *Climate Dyn.*, **46**, 3007–3023, https://doi.org/10.1007/s00382-015-2749-0.

Jin, F.-F., 1997: An equatorial ocean recharge paradigm for ENSO. Part I: Conceptual model. *J. Atmos. Sci.*, **54**, 811–829, https://doi.org/10.1175/1520-0469(1997)054<0811:AEORPF>2.0.CO;2.

Kao, H.-Y., and J.-Y. Yu, 2009: Contrasting eastern-Pacific and central-Pacific types of ENSO. *J. Climate*, **22**, 615–632, https://doi.org/10.1175/2008JCLI2309.1.

Kug, J.-S., F.-F. Jin, and S.-I. An, 2009: Two types of El Niño events: Cold tongue El Niño and warm pool El Niño. *J. Climate*, **22**, 1499–1515, https://doi.org/10.1175/2008JCLI2624.1.

Larson, S. M., and B. P. Kirtman, 2014: The Pacific meridional mode as an ENSO precursor and predictor in the North American multimodel ensemble. *J. Climate*, **27**, 7018–7032, https://doi.org/10.1175/JCLI-D-14-00055.1.

——, and ——, 2015: Revisiting ENSO coupled instability theory and SST error growth in a fully coupled model. *J. Climate*, **28**, 4724–4742, https://doi.org/10.1175/JCLI-D-14-00731.1.

——, and ——, 2017: Drivers of coupled model ENSO error dynamics and the spring predictability barrier. *Climate Dyn.*, **48**, 3631–3644, https://doi.org/10.1007/s00382-016-3290-5.

——, and ——, 2019: Linking preconditioning to extreme ENSO events and reduced ensemble spread. *Climate Dyn.*, **52**, 7417–7433, https://doi.org/10.1007/s00382-017-3791-x.

——, D. J. Vimont, A. C. Clement, and B. P. Kirtman, 2018a: How momentum coupling affects SST variance and large-scale Pacific climate variability in CESM. *J. Climate*, **31**, 2927–2944, https://doi.org/10.1175/JCLI-D-17-0645.1.

——, K. V. Pegion, and B. P. Kirtman, 2018b: The South Pacific meridional mode as a thermally driven source of ENSO amplitude modulation and uncertainty. *J. Climate*, **31**, 5127–5145, https://doi.org/10.1175/JCLI-D-17-0722.1.

Lau, N.-C., and M. J. Nath, 1996: The role of the "atmospheric bridge" in linking tropical Pacific ENSO events to extratropical SST anomalies. *J. Climate*, **9**, 2036–2057, https://doi.org/10.1175/1520-0442(1996)009<2036:TROTBI>2.0.CO;2.

Lee, S.-K., H. Lopez, E.-S. Chung, P. DiNezio, S.-W. Yeh, and A. T. Wittenberg, 2018: On the fragile relationship between El Niño and California rainfall. *Geophys. Res. Lett.*, **45**, 907–915, https://doi.org/10.1002/2017GL076197.

Lin, C.-Y., J.-Y. Yu, and H.-H. Hsu, 2015: CMIP5 model simulations of the Pacific meridional mode and its connection to the two types of ENSO. *Int. J. Climatol.*, **35**, 2352–2358, https://doi.org/10.1002/joc.4130.

Lu, F., Z. Liu, Y. Liu, S. Zhang, and R. Jacob, 2017: Understanding the control of extratropical atmospheric variability on ENSO using a coupled data assimilation approach. *Climate Dyn.*, **48**, 3139–3160, https://doi.org/10.1007/s00382-016-3256-7.

McPhaden, M. J., 2015: Playing hide and seek with El Niño. *Nat. Climate Change*, **5**, 791–795, https://doi.org/10.1038/nclimate2775.

Meinen, C. S., 2000: Observations of warm water volume changes in the equatorial Pacific and their relationship to El Niño and La Niña. *J. Climate*, **13**, 3551–3559, https://doi.org/10.1175/1520-0442(2000)013<3551:OOWWVC>2.0.CO;2.

Montégut, C. B., J. Vialard, S. S. C. Shenoi, D. Shankar, F. Durand, C. Ethé, and G. Madec, 2007: Simulated seasonal and interannual variability of the mixed layer heat budget in the northern Indian Ocean. *J. Climate*, **20**, 3249–3268, https://doi.org/10.1175/JCLI4148.1.

Pegion, K., and M. Alexander, 2013: The seasonal footprinting mechanism in CFSv2: Simulation and impact on ENSO prediction. *Climate Dyn.*, **41**, 1671–1683, https://doi.org/10.1007/s00382-013-1887-5.

——, C. M. Selman, S. Larson, J. C. Furtado, and E. J. Becker, 2020: The impact of the extratropics on ENSO diversity and predictability. *Climate Dyn.*, **54**, 4469–4484, https://doi.org/10.1007/s00382-020-05232-3.

Rogers, J. C., 1981: The North Pacific oscillation. *J. Climatol.*, **1**, 39–57, https://doi.org/10.1002/joc.3370010106.

Santoso, A., M. J. Mcphaden, and W. Cai, 2017: The defining characteristics of ENSO extremes and the strong 2015/2016 El Niño. *Rev. Geophys.*, **55**, 1079–1129, https://doi.org/10.1002/2017RG000560.

Smith, R., and Coauthors, 2010: The Parallel Ocean Program (POP) reference manual. Los Alamos National Laboratory Tech. Rep. LAUR-10-01853, 141 pp.

Tippett, M. K., A. G. Barnston, and S. Li, 2012: Performance of recent multimodel ENSO forecasts. *J. Appl. Meteor. Climatol.*, **51**, 637–654, https://doi.org/10.1175/JAMC-D-11-093.1.

Brought to you by NOAA Central Library | Unauthenticated | Downloaded 10/12/21 03:47 PM UTC

Trenberth, K. E., 1997: The definition of El Niño. *Bull. Amer. Meteor. Soc.*, **78**, 2771–2777. https://doi.org/10.1175/1520-0477(1997)078,2771:TDOENO.2.0.CO;2.

Vimont, D. J., D. S. Battisti, and A. C. Hirst, 2003: The seasonal footprinting mechanism in the CSIRO general circulation models. *J. Climate*, **16**, 2653–2667, https://doi.org/10.1175/1520-0442(2003)016<2653:TSFMIT>2.0.CO;2.

——, M. Alexander, and A. Fontaine, 2009: Midlatitude excitation of tropical variability in the Pacific: The role of thermodynamic coupling and seasonality. *J. Climate*, **22**, 518–534, https://doi.org/10.1175/2008JCLI2220.1.

Wang, P., C.-Y. Tam, and K. Xu, 2019: El Niño–East Asian monsoon teleconnection and its diversity in CMIP5 models. *Climate Dyn.*, **53**, 6417–6435, https://doi.org/10.1007/s00382-019-04938-3.

Wang, X., M. Chen, C. Wang, S. Yeh, and W. Tan, 2019: Evaluation of performance of CMIP5 models in simulating the North Pacific oscillation and El Niño Modoki. *Climate Dyn.*, **52**, 1383–1394, https://doi.org/10.1007/s00382-018-4196-1.

Wang, Z., L. Han, J. Zheng, R. Ding, J. Li, Z. Hou, and J. Chao, 2021: Evaluation of the performance of CMIP5 and CMIP6 models in simulating the Victoria mode–El Niño relationship. *J. Climate*, **34**, 7625–7644, https://doi.org/10.1175/JCLI-D-20-0927.

Wyrtki, K., 1985: Water displacements in the Pacific and the genesis of El Niño cycles. *J. Geophys. Res.*, **90**, 7129, https://doi.org/10.1029/JC090iC04p07129.

Xie, R., and F.-F. Jin, 2018: Two Leading ENSO modes and El Niño types in the Zebiak–Cane model. *J. Climate*, **31**, 1943–1962, https://doi.org/10.1175/JCLI-D-17-0469.1.

Yu, J.-Y., and S. T. Kim, 2010: Three evolution patterns of Central-Pacific El Niño. *Geophys. Res. Lett.*, **37**, L08706, https://doi.org/10.1029/2010GL042810.

——, and ——, 2011: Relationships between extratropical sea level pressure variations and the central Pacific and eastern Pacific types of ENSO. *J. Climate*, **24**, 708–720, https://doi.org/10.1175/2010JCLI3688.1.

——, X. Wang, S. Yang, H. Paek, and M. Chen, 2017: Changing El Niño–Southern Oscillation and associated climate extremes. *Climate Extremes: Patterns and Mechanisms*, *Geophys. Monogr.*, Vol. 226, Amer. Geophys. Union, 3–38.

Brought to you by NOAA Central Library | Unauthenticated | Downloaded 10/12/21 03:47 PM UTC